

AperTO - Archivio Istituzionale Open Access dell'Università di Torino

Facile synthesis of ZnO nano-structures: Morphology influence on electronic properties

This is the author's manuscript

Original Citation:

Availability:

This version is available <http://hdl.handle.net/2318/1645569> since 2023-11-17T09:20:31Z

Published version:

DOI:10.1016/j.snb.2017.03.114

Terms of use:

Open Access

Anyone can freely access the full text of works made available as "Open Access". Works made available under a Creative Commons license can be used according to the terms and conditions of said license. Use of all other works requires consent of the right holder (author or publisher) if not exempted from copyright protection by the applicable law.

(Article begins on next page)

Facile synthesis of ZnO nano-structures: morphology influence on electronic properties

S. Morandi^{1*}, A. Fioravanti^{2,3}, G. Cerrato¹, S. Lettieri⁴, M. Sacerdoti⁵, M. C. Carotta²

¹ *Dipartimento di Chimica and NIS, Inter-departmental Center, Università di Torino, Via
Pietro Giuria 7, 10125 Torino, Italy.*

² *Laboratorio Sensori e Nanomateriali, CNR – IMAMOTER, Via Canal Bianco 28, Ferrara,
Italy.*

³ *Dipartimento di Chimica, Università di Parma, Parco Area delle Scienze 17A, 43124
Parma, Italy.*

⁴ *Institute of Applied Sciences and Intelligent Systems E. Caianiello, CNR-ISASI, Via
Campi Flegrei 34, Pozzuoli (NA), Italy.*

⁵ *Dipartimento di Fisica e Scienze della Terra, Università di Ferrara, Via Saragat 1, 44122
Ferrara, Italy.*

**Corresponding author: Tel. +390116707539, Fax: +390116707855; e-mail address:
sara.morandi@unito.it*

Abstract

ZnO samples with different nano-structures were synthesized by a facile method in which solutions containing zinc nitrate, ammonium hydroxide or hexamethylenetetramine were heated at different temperatures. Along with morphological and structural analysis, electrical and spectroscopic characterizations have been performed to investigate the role played by the sample morphologies. The spectroscopic results obtained during interaction with acetone well correlate with the electrical measurements: the higher is the intensity of the electronic absorptions in IR spectra, the higher is the electrical response to the tested gas. In particular, samples constituted by particles with well defined and smoothed surfaces are characterized only by the increase of electron population in the conduction band caused by acetone interaction and show peculiar energy barrier features. Samples constituted by particles with indented surfaces give the increase of electron population both in the conduction band and in oxygen vacancies. These last samples show similar energy barrier features.

Key words: ZnO nano-structures, metal oxide gas sensors, acetone, FT-IR

1. Introduction

ZnO nano-structures are characterized by low toxicity, good thermal stability, good biocompatibility, large specific surface area, transparency and high electron mobility, which make ZnO suitable for various applications such as blue and UV light-emitting diodes, photodetectors, solar cells, field effect transistors, gas and bio-sensors [1]. The morphology-controlled synthesis of ZnO nano-structures was extensively studied, being able to form nano-rods, nano-tubes, nano-needles, nano-disks simply by adjusting preparation method and conditions [2-4]. In this frame, much attention has been put on ZnO nano-structures for sensing applications: the morphology control of nano-sized metal oxide semiconductors can be envisaged to improve the selectivity towards various gases [5-7].

Recently, breath gas analysis has attracted much attention as a non-invasive detection of diseases in the evaluation of human health [8, 9]. The breath analysis is today carried out through bulky and expensive instruments, thereby low cost and easy to use devices such as solid state sensors could be an alternative to analytical techniques to analyze the exhaled breath in real-time [10]. In particular, acetone is a natural biomarker correlated with some metabolic diseases, like the diabetes and the diabetic ketoacidosis. With this aim in view, in this work ZnO samples in form of nano-particle aggregates and bi-dimensional nano-crystals with different shapes were synthesized through sol-gel processes and all the sensing films were tested toward acetone and other VOCs related to the breath gas analysis such as acetaldehyde, ethanol and ammonia.

Moreover, FT-IR spectroscopy was performed during the interaction with acetone at increasing temperature in order to study the electronic properties of the different samples. It

was possible to correlate electrical and spectroscopic results with the morphology features of the samples analyzed by Scanning and Transmission Electron microscopy (SEM and TEM) measurements.

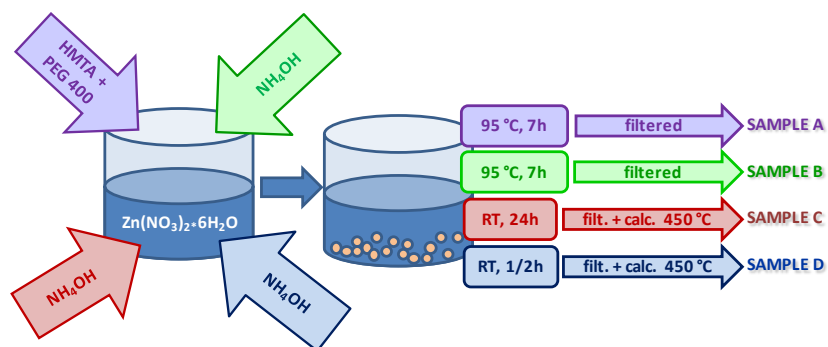
2. Materials and methods

Zinc oxide samples with different morphologies were synthesized through sol-gel processes. In particular, four different morphologies, named A, B, C and D, were obtained starting from $\text{Zn}(\text{NO}_3)_2 \cdot 6\text{H}_2\text{O}$ ($\geq 99.0\%$, Sigma-Aldrich) in aqueous solution. For the preparation of sample A, a water solution 0.1 M of $\text{Zn}(\text{NO}_3)_2 \cdot 6\text{H}_2\text{O}$ and one 0.05 M of hexamethylenetetramine (HMTA) were prepared and mixed under continuous stirring. A small amount (0.1 mol% with respect to $\text{Zn}(\text{NO}_3)_2 \cdot 6\text{H}_2\text{O}$) of polyethyleneglycol (PEG, MW = 400) was next added after mixing. The mixture was then kept at the temperature of 95 °C for 7 hours. The precipitate was filtered by gravity, washed several times with water and diethyl ether, before drying at 100 °C in air overnight in oven.

Samples B, C and D were prepared adding a proper amount of ammonium hydroxide (28%, Carlo Erba Reagents) to a water solution 0.05 M of $\text{Zn}(\text{NO}_3)_2 \cdot 6\text{H}_2\text{O}$, bringing the solution pH to 10. Sample B was then kept at the temperature of 95 °C for 7 hours. The precipitate was filtered, washed several times with water and diethyl ether, before drying at 100 °C in air overnight. Samples D and C were obtained aging at room temperature the solution for 1 hour or 24 hours, respectively. The precipitates were filtered, washed several times with water and diethyl ether, dried at 100 °C overnight and then calcined at 450 °C

for 2 h. In Scheme 1 a pictorial description of the sample syntheses is reported for sake of clarity.

Scheme 1. Pictorial description of the sample syntheses.



It is worth of note that samples A and B were directly obtained as ZnO after the precipitation in the solutions, otherwise, samples C and D were obtained as the $\epsilon\text{-Zn}(\text{OH})_2$ precursor with different morphologies. Through a subsequent calcination, different forms of ZnO were achieved.

X-ray diffraction (XRD) patterns of the samples were collected on a PW 3830/3020 X'Pert Diffractometer from PANalytical working with Bragg-Brentano geometry, using the $\text{Cu K}\alpha_1$ radiation ($\lambda = 1.5406 \text{ \AA}$). Average crystallite size values were calculated by applying the Scherrer's formula on the (101) diffraction peak in the diffractograms.

The specific surface areas of the samples were determined by applying the Brunauer-Emmett-Teller (BET) method to the adsorption/desorption isotherms of N_2 at 77 K obtained with a Micromeritics ASAP 2010 physisorption analyzer.

Morphological characterization of the samples was performed by: (i) Field Emission Scanning Electron Microscopy (FE-SEM) using a Carl Zeiss Sigma microscope; (ii) Transmission Electron Microscopy (TEM) and High Resolution (HR)-TEM using a side entry Jeol JEM 3010 (300 kV) microscope equipped with a LaB₆ filament. For TEM analyses, the samples were deposited on a copper grid, coated with a porous carbon film; the digital micrographs were acquired by an Ultrascan 1000 camera and the images were processed by Gatan digital micrograph.

Absorption/transmission IR spectra were run on a Perkin-Elmer FTIR System 2000 spectrophotometer equipped with a Hg-Cd-Te cryo-detector, working in the range of wavenumbers 7200-580 cm⁻¹ at a resolution of 2 cm⁻¹. For IR analysis powder samples were compressed in self-supporting discs (10 mg cm⁻²) and placed in a commercial heated stainless steel cell (Aabspec) allowing thermal treatments in situ under vacuum or controlled atmosphere and the simultaneous registration of spectra at temperatures up to 600 °C. Before the measurements, the samples were treated at 400 °C in vacuum and dry oxygen in order to clean the surface from adsorbed species and to maintain ZnO well oxidized. After this activation stage, the samples were cooled down to 50 °C in oxygen and outgassed before the admission of a mixture acetone/O₂ (1:5, p_{acetone} = 5 mbar). The IR spectra were recorded during the interaction with the mixture at increasing temperature up to 400 °C. The recorded spectra are reported as difference spectra in the figures: the spectrum subtracted is always that recorded after the activation treatment in oxygen at the same temperatures used for studying acetone interaction. In this way the modifications induced by acetone and the surface species formed are put in evidence.

In order to perform electrical measurements, thick films constituted by the ZnO powders were deposited through screen printing technique onto miniaturized alumina substrates suited for conductometric analysis, each one provided with a heater element and interdigitated electrodes. To print the sensing layers, a viscous paste was prepared by adding to the functional material an organic vehicle and a small amount of a bonding agent to promote the film adhesion to the alumina substrate. The films were then fired at 650 °C for 1 h in a muffle furnace. The sensors were placed in a sealed test chamber maintained at a fixed ambient temperature of 20 °C to avoid the influence of it on the sensor behavior [11]. The flow-through technique was used to test the electrical properties of the sensing layers, maintaining a flow rate of 0.5 L/min using synthetic air as carrier gas in dry conditions. Dynamical responses of the sensing films were obtained in presence of the gases of interest by varying the working temperature from 350 to 550 °C. The sensor response is defined as ratio between the conductance in presence of the target gas and the conductance in air.

The determination of the height of the surface potential barrier is carried out measuring the conductance by changing the temperature between 300 and 900 °C at the heating rate of 3 °C/min. Afterwards, the conductance is measured at a fixed temperature as a function of time, after a change of temperature so fast that it is possible to assume the constancy of the barrier while the conductance changes due to the variation of free carriers. Finally, through Morrison's equation which takes into account the surface and bulk contributions, the heights of the potential barrier as a function of temperature can be calculated from the measured conductance values [12].

3. Results and discussion

3.1 Textural, structural and morphological characterization

XRD patterns of all the samples are characteristic of ZnO with hexagonal wurtzite-like structure ($P6_3mc$), as shown in Figure 1 for sample D. Average crystallite sizes calculated by the Scherrer's formula applied on the (101) diffraction peaks are reported in Table 1: the crystallite size gradually decreases passing from 66 nm for sample A to 26 nm for sample D. Samples A, B and C show very similar specific surface areas, about 11-13 m^2/g (Table1); sample D exhibits a quite higher SSA with respect to the other samples (19 m^2/g).

Table 1. Average crystallite sizes and specific surface areas of the ZnO samples.

Sample	Ave. cryst. size (nm)	SSA (m^2/g)
A	46	11
B	36	13
C	33	12
D	26	19

FE-SEM analysis reported in Figure 2 clearly reveals the different morphologies of the samples. Samples A and B appear to be constituted by elongated particles: on one hand, sample A is characterized by hexagonal prisms about 50-150 nm wide with well defined and smoothed surfaces, as evidenced in the inset of Figure 2A; on the other hand, the acicular particles of sample B show highly indented surfaces, as well evident in the inset of

Figure 2B, and very large distributions of width and length. Sample C is constituted by porous bisphenoids in which the fine structure, reported in the inset of Figure 2C, highlights the presence of roundish nano-particles, whose sizes are highly inhomogeneous. Sample D is characterized by sheets of rhombic shape with a fine structure, reported in the inset of Figure 2D, given by roundish nano-particles whose sizes are highly homogeneous (about 60-70 nm). As a matter of fact, samples A and B are constituted by nano-particles aggregates.

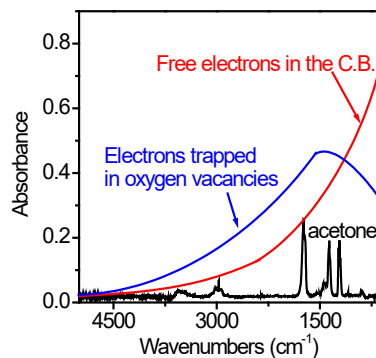
Among all the specimens, only sample A appears to be constituted by highly defined particles with smoothed surfaces and regular shape. In agreement with this characteristic, in the following both electrical and spectroscopic measurements reveal peculiar behaviors of sample A (vide infra). In order to deepen the morphological characterization of this sample, TEM and HR-TEM images were collected and few of them are reported in Figure 3. HR-TEM images (Fig. 3 sections b and c) well show that only one kind of interference fringes related to the (002) planes (inter-planar distance = 2.43 Å) are present across all the hexagonal prism section, demonstrating that the prisms of sample A are mono-crystals. There is an apparent disagreement between the average crystallite size calculated by the Scherrer's formula and the TEM and HR-TEM observations reporting images of mono-crystals of several hundreds of nanometers. However, it must be taken into account that the estimation of the crystallite length through the Scherrer's formula is the length of the almost perfect crystal. As a matter of fact, the rapid crystallization of the sample A is reasonably accompanied by the formation of different defects, such as dislocations, stacking faults, etc. in a large quantity. Thereby, the average crystallite size can be considered as an average

distance between the growth defects due to the rapid crystallization implied in the specific synthesis method.

3.2 Spectroscopic characterization

In Figure 4 FT-IR spectra of the samples in interaction with acetone/O₂ mixture at increasing temperature are reported. From a general point of view, the spectra are characterized by the increase of electronic absorptions related to: (i) the transition of electrons from mono-ionized oxygen vacancies to the conduction band (CB); (ii) free electrons in the CB [13, 14]. The characteristic shapes of these absorptions are represented in Scheme 2: free electrons in the CB are characterized by a monotonic absorption that increases in intensity on decreasing the wavenumbers (red curve); the electronic transition from mono-ionized oxygen vacancies to the CB gives a very broad band centered at wavenumbers that correspond to the energy separation between the electronic levels related to mono-ionized oxygen vacancies and the bottom of the CB (blue curve). In the case of ZnO, the energy of ionization of mono-ionized oxygen vacancies is known to be 0.18 eV [15], which corresponds to a band centered at about 1500 cm⁻¹. For all the samples the observed electronic absorptions (Fig. 4) increase in intensity on increasing temperature up to 350 °C due to the reaction of acetone with surface oxygen species (O₂⁻, O⁻, O²⁻) that injects electrons in the CB and in bi-ionized oxygen vacancies of ZnO. At 400 °C the observed electronic absorptions decrease in intensity due to partial re-oxidation of the surface operated by oxygen in the mixture.

Scheme 2. Pictorial representation of the IR absorption bands related to free electrons in the CB (red curve) and to the transition of electrons from mono-ionized oxygen vacancies to the CB (blue curve). IR spectrum of acetone vapor is also reported (black curve).



The bands related to the vibrational modes of acetone in the gas phase, whose IR spectrum is reported in Scheme 2 (black curve), are superimposed to the broad bands related to the electronic absorptions described above. The acetone vibrational bands decrease in intensity on increasing temperature, being acetone consumed by the surface reaction occurred with surface oxygen species. For all the samples, starting from 150-200 °C, two bands related to vibrational modes of surface carbonates at 1440 and 1550 cm⁻¹ are formed and increase in intensity on increasing temperature. Carbonate species arise from the chemisorption of CO₂, which is formed by the acetone oxidation. CO₂ formation in the gas phase is revealed by the roto-vibrational band at 2341 cm⁻¹.

Down in the detail of individual specimen, for sample A (Fig. 4, section A) the interaction with acetone causes only the formation of the absorption related to free electrons in the CB. The band related to the photo-ionization of mono-ionized oxygen

vacancies is not observed. This behavior distinguishes sample A from all the other samples, for which both the absorption related to free electrons and that related to mono-ionized oxygen vacancies are observed (Fig. 4 sections B, C and D). The reason for the observed difference can be searched in the different sample morphologies: the presence of intrinsic surface defects, such as oxygen vacancies able to trap electrons, is guaranteed by materials showing badly defined crystallites with indented borders, such as samples B, C and D [16]. The highly defined mono-crystals of sample A do not guarantee a sufficient amount of surface oxygen vacancies for IR detection.

As for sample B, C and D, the ratio between the intensity of the absorption related to free electrons and that related to mono-ionized oxygen vacancies increases passing from sample B to sample D. For sample D the band associated to oxygen vacancies is dominant, in agreement with SEM analysis that shows the presence of smaller and, as a consequence, more defective particles for this last specimen.

As for the overall integrated intensity of the electronic absorptions, samples A and D exhibits higher values with respect to samples B and C, in agreement with electrical measurements that reveal higher response to acetone for samples A and D, as reported below. Moreover, sample B shows the lowest electronic absorption intensity, well in agreement with the worst sensitivity to acetone (*vide infra*).

3.3 Electrical characterization

The semiconductor oxides of n-type are characterized by the presence of free electrons in the conduction band mainly due to lattice defects, such as oxygen vacancies. The conductance model, generally accepted for gas sensors based on polycrystalline n-type

semiconductors, is based on the Schottky barrier formation at gas-semiconductor interface and it is attributed to a negative surface charge accumulation, typically O_2^- , O^- ions. In nanocrystalline semiconductors, the mechanism of conduction is controlled by the presence of a huge series of intergranular point contacts at which the surface barrier develops, due to the presence of charged surface states. Conductance therefore is an activated process, since only those electrons with sufficient energy to cross the barrier take part to electrical conductance [11]. The gas sensing mechanism is based on the variation of the potential barrier height as a result of surface chemical reactions with environmental gases, leading to the electrical conductance modification.

Starting with this peculiar mechanism, a lot of features determine the sensor performance, but certainly the grain size reduction at nanometric level is one of the main factors enhancing their detection properties [17-19], both for large specific surface offered and for the influence in reducing the surface charge density. Indeed, when the particle dimensions scale down below a critical value, the phenomenon of the unpinning of Fermi level occurs, thus improving the sensor response of these materials [20]. Apart from the grain size reduction, a lot of other complex factors affect the sensor performance which, in turn, is determined by the reception and transduction functions [21]. The selection of the functional material, the synthesis procedure, crystal size and shape, the addition of foreign elements with the role of sensitizers or conductivity modifiers are the key factors which determine the sensor response toward a specific gas.

On the base of the conductance model above described, the Arrhenius plots, reported in Figure 5, evidence that all samples exhibit n-type semiconductor-like behavior modulated

by the Schottky barrier formation at gas-semiconductor interface. As regards the conductivity values, no particular difference between the samples can be found.

However, a different situation is offered by the measures of the energy barrier heights in air and their trends as a function of temperature (Fig. 6). In fact, looking at the two types of morphologies (aggregates of roundish nano-particles for the samples C and D; elongated nano-crystals for the samples A and B), a peculiar feature can be observed: while the sample D exhibits a higher energy barrier and higher responses to reducing gases (see the next section) than the sample C, different is the situation of the samples A and B, for which this order is not observed. It is well known that the spherical geometry of the particles, favoring the barrier formation [22], causes the classical behavior with higher gas responses corresponding to a higher SSA (see Table 1) in turn leading to a higher barrier height. Obviously, this situation is true until the grain radius is greater than the depletion layer width. Otherwise, the samples A and B, constituted by elongated particles, don't follow this behavior. Indeed, the energy barrier of the sample A in air is much lower and different in shape than the one of the sample B, being however the responses to reducing gases higher for the sample A characterized by a lower barrier.

This fact can be also observed in Figure 7, where the comparison between the energy barriers in air and in 10 ppm of acetone is reported. The difference between the height of the energy barrier measured in acetone and in air of the sample D, taken as representative of the samples having roundish nano-particle morphology, is much wider than in the two samples characterized by elongated nano-crystal morphologies. It means that in the sample D a great amount of electrons participates to the detection process, thus promoting the gas response. Looking at the behavior of the samples A and B, the sample A, characterized by

nano-particles in form of hexagonal prisms, exhibits a much wider difference between the energy barriers in air and in acetone than the sample B, thus confirming what observed above. However, on the basis of the described results and on the Schottky barrier model, the differences between the barriers of the samples A and B are not explainable. At first sight, one might ascribe the low barrier height of the sample A to the effect of band-bending flattening [23]. On the other hand, the hexagonal prism size is certainly larger than the characteristic width of the depletion layer. Thereby, the low energy barrier could instead be related to a low density of surface states, in particular due to a poor amount of surface oxygen vacancies, in agreement with the results obtained by SEM and HR-TEM analysis. In fact, the hexagonal prisms of which the sample A is constituted, exhibit highly crystalline surfaces that do not favor atomic adsorption. Moreover, as reported in section 3.2, FT-IR measurements show that the interaction with acetone causes the formation of only the absorption related to free electrons in the CB and not of the band related to the photo-ionization of mono-ionized oxygen vacancies. This is reasonably the cause of the different behavior between the samples A and B. Effectively, although both samples are formed by elongated crystals, the needles of sample B exhibit crystalline surfaces less defined and borders much less regular of the ones of the sample A.

3.4 Gas sensing properties

The main features of the gas sensing properties of the examined samples can be pointed out as follows: i) all sensors exhibit the best response toward acetone, as shown in Figure 8, where the responses to 10 ppm of all tested gases in dry air are reported. Here, the response toward a specific gas has been reported at the operating temperature for which the response

resulted maximized; ii) showing all samples a good selectivity toward acetone with respect to other VOCs, such as ammonia, ethanol and acetaldehyde typical of breath gas analysis, the different morphologies of zinc oxide seem not affect the surface chemistry; iii) on the contrary, the morphology strongly influence the sensitivity, the sample D and C offering the best responses toward acetone. In particular, the sample D, characterized by sheets of rhombic shape with a fine structure of nano-particles (about 60-70 nm), shows greater responses than the sample C composed by bisphenoids with particles affected by moderate coalescence; iv) surprisingly, the sample A, constituted by highly defined particles (hexagonal prisms) with smoothed surfaces and regular shape, exhibits an excellent response to acetone (as shown in Figure 9), differently from other bi-dimensional crystals (as for example sample B), offering a much more poor gas response. This experimental evidence has been already detected and reported in previous results of some of the authors of the present work (see eg [24, 25]). Effectively, this feature would be expected because the Schottky barrier formation is favoured in spherical geometry with respect to a planar one [22]. Moreover, as proved by FTIR analysis (formation of only the absorption related to free electrons in the CB caused by interaction with acetone), this particular phenomenon is thereby to ascribe to a more complex sensing mechanism, so hypothesized for the sample A: the acetone detection occurs through surface lattice oxygens rather than chemisorbed ones, permitting the electrons to enter in the conduction band after the reaction, thus contributing to the detection process without affecting the barrier height.

Finally, in Figure 10, dynamical responses of all sensors toward acetone concentrations ranging from 10 to 0.5 ppm in dry air is reported. Other characterizations, not shown here, proved that such sensors are able to detect acetone concentrations down to few tens of ppb.

Table 2. Response and recovery times of the sensors compared with SSA of their functional materials.

Sample	Response time (min)	Recovery time (min)
A	3.0	6.1
B	3.0	6.0
C	5.0	6.4
D	4.6	6.3

Very important parameters in real time detectors are electrical stability as well as response and recovery times (RRTs). Concerning the electrical stability, thick film sensors have been fired at a sufficiently high temperature to provide the sensor response with a completely satisfactory stability, as long as the ambient conditions do not vary [11]. Hereinafter, RRTs will be shown for the samples examined in this work. However, to quantitatively compare them with those of other authors, it would be necessary to know the characteristics of the various measurement apparatus. Indeed, in [26] it has been demonstrated that RRTs are much dependent on the test chamber volume than the sensor characteristics. In particular, more the chamber volume is reduced, more RRTs resulted lowered.

In Table 2, RRTs of all examined sensors are summarized and compared with SSA with the corresponding functional materials. Concerning the response time, the sensors A and B exhibit a lower response time with respect to samples C and D characterized by morphology consisting in roundish nano-particles. It means that the particles in form of elongated nano-crystals offer defined surfaces with well accessible sites.

On the other hand, the recovery times don't show significant differences, showing that further mechanisms, as for instance the rate of the re-adsorption of oxygen on ZnO surface, play a prevalent role.

4. Conclusions

A series of ZnO samples were synthesized by a facile method in which solutions containing zinc nitrate, ammonium hydroxide or hexamethylenetetramine were heated at different temperatures. Among the synthesized specimens, one sample (sample A) appears to be constituted by highly defined mono-crystals with smoothed surfaces and regular shape. The other three samples are constituted by particles with irregular and indented surfaces. These morphological characteristics are reflected into two different behaviors during acetone interaction studied by FT-IR spectroscopy: (i) sample A is characterized only by the increase of electron population in the CB; (ii) the other three samples give the increase of electron population both in the CB and in the oxygen vacancies. Accordingly, these last samples show similar energy barrier features that are different from that of sample A. The reason for the observed difference can be understood in the different morphologies of the samples: the presence of intrinsic surface defects, such as oxygen vacancies able to trap electrons, is guaranteed by materials showing badly defined crystallites with indented borders and not by the sample with well defined and smoothed surfaces. The ratio between electron population in oxygen vacancies and in CB increases passing from sample B to

sample D, in agreement with SEM analysis that shows the presence of smaller and, as a consequence, more defective particles for sample D.

Spectroscopic results well correlate with electrical measurements: the higher is the intensity of the electronic absorption in IR spectra, the higher is the electrical response to acetone. In particular, samples A and D show the most intense electronic absorptions in the FT-IR spectra and the highest electrical responses to acetone.

Acknowledgements

We sincerely acknowledge Dr. Mauro Mazzocchi (CNR-ISTEC, Faenza, Italy) for performing SEM analyses on ZnO powders.

References

- [1] A. Wei, L.H. Pan, W. Huang, Recent progress in the ZnO nanostructure-based sensors, *Mater. Sci. Eng. B* 176(18) (2011) 1409-1421.
- [2] S. Cho, S.H. Jung, J.W. Jang, E. Oh, K.H. Lee, Simultaneous Synthesis of Al-Doped ZnO Nanoneedles and Zinc Aluminum Hydroxides through Use of a Seed Layer, *Cryst. Growth Des.* 8(12) (2008) 4553-4558.
- [3] S.W. Kan, S.K. Mohanta, Y.Y. Kim, H.K. Cho, Realization of vertically well-aligned ZnO : Ga nanorods by magnetron sputtering and their field emission behavior, *Cryst. Growth Des.* 8(5) (2008) 1458-1460.
- [4] Y.C. Chang, W.C. Yang, C.M. Chang, P.C. Hsu, L.J. Chen, Controlled Growth of ZnO Nanopagoda Arrays with Varied Lamination and Apex Angles, *Cryst. Growth Des.* 9(7) (2009) 3161-3167.
- [5] A. Ryzhikov, J. Jonca, M. Kahn, K. Fajerweg, B. Chaudret, A. Chapelle, P. Menini, C.H. Shim, A. Gaudon, P. Fau, Organometallic synthesis of ZnO nanoparticles for gas sensing: towards selectivity through nanoparticles morphology, *J. Nanopart. Res.* 17(7) (2015).
- [6] N. Song, H. Fan, H. Tian, PVP assisted in situ synthesis of functionalized graphene/ZnO (FGZnO) nanohybrids with enhanced gas-sensing property, *J. Mater. Sci.* 50(5) (2015) 2229-2238.
- [7] H. Tian, H. Fan, M. Li, L. Ma, Zeolitic Imidazolate Framework Coated ZnO Nanorods as Molecular Sieving to Improve Selectivity of Formaldehyde Gas Sensor, *ACS Sensors* 1(3) (2016) 243-250.
- [8] A. Amann, B. Costello, W. Miekisch, J. Schubert, B. Buszewski, J. Pleil, N. Ratcliffe, T. Risby, The human volatilome: volatile organic compounds (VOCs) in exhaled breath, skin emanations, urine, feces and saliva, *J. Breath Res.* 8(3) (2014).
- [9] K.H. Kim, S.A. Jahan, E. Kabir, A review of breath analysis for diagnosis of human health, *Trends Anal. Chem.* 33 (2012) 1-8.

- [10] I.-D. Kim, S.-J. Choi, S.-J. Kim, J.-S. Jang, Exhaled Breath Sensors, C.-M. Kyung (Ed.), Smart Sensors for Health and Environment Monitoring KAIST Research Series (DOI: 10.1007/978-94-017-9981-2_2) (2015).
- [11] M.C. Carotta, M. Benetti, E. Ferrari, A. Giberti, C. Malagu, M. Nagliati, B. Vendemiati, G. Martinelli, Basic interpretation of thick film gas sensors for atmospheric application, *Sens. Actuators B: Chem.* 126(2) (2007) 672-677.
- [12] V. Lantto, P. Romppainen, S. Leppavuori, A study of the temperature dependence of the barrier energy in porous tin dioxide, *Sens. Actuators* 14 (1988) 149-163.
- [13] G. Ghiotti, A. Chiorino, F. Boccuzzi, Surface-chemistry and electronic effects of H₂ (D₂) on 2 different microcrystalline ZnO powders, *Surf. Sci.* 287 (1993) 228-234.
- [14] A. Chiorino, G. Ghiotti, F. Prinetto, M.C. Carotta, C. Malagu, G. Martinelli, Preparation and characterization of SnO₂ and WO_x-SnO₂ nanosized powders and thick films for gas sensing, *Sens. Actuators B: Chem.* 78(1-3) (2001) 89-97.
- [15] U.L. W. Gopel, Influence of defects on the electronic structure of zinc oxide surfaces *Phys. Rev. B* 22 (1980) 15.
- [16] A. Chiorino, G. Ghiotti, F. Prinetto, M.C. Carotta, G. Martinelli, M. Merli, Characterization of SnO₂-based gas sensors. A spectroscopic and electrical study of thick films from commercial and laboratory-prepared samples, *Sens. Actuators B: Chem.* 44(1-3) (1997) 474-482.
- [17] C.N. Xu, J. Tamaki, N. Miura, N. Yamazoe, Grain-size effects on gas sensitivity of porous SnO₂-based elements
Sens. Actuators B: Chem. 3(2) (1991) 147-155.
- [18] X.J. Huang, Y.K. Choi, Chemical sensors based on nanostructured materials, *Sens. Actuators B: Chem.* 122(2) (2007) 659-671.
- [19] K.J. Choi, H.W. Jang, One-Dimensional Oxide Nanostructures as Gas-Sensing Materials: Review and Issues, *Sensors* 10(4) (2010) 4083-4099.
- [20] C. Malagu, V. Guidi, M. Stefancich, M.C. Carotta, G. Martinelli, Model for Schottky barrier and surface states in nanostructured n-type semiconductors, *J. Appl. Phys.* 91(2) (2002) 808-814.

- [21] N. Yamazoe, K. Shimano, Receptor Function and Response of Semiconductor Gas Sensor, *J. Sensors* ID 875704 (2009).
- [22] E. Comini, V. Guidi, C. Malagu, G. Martinelli, Z. Pan, G. Sberveglieri, Z.L. Wang, Electrical properties of tin dioxide two-dimensional nanostructures, *J. Phys. Chem. B* 108(6) (2004) 1882-1887.
- [23] M.C. Carotta, A. Fioravanti, S. Gherardi, C. Malagu, M. Sacerdoti, G. Ghiotti, S. Morandi, (Ti,Sn) solid solutions as functional materials for gas sensing, *Sens. Actuators B: Chem.* 194 (2014) 195-205.
- [24] A. Fioravanti, A. Bonanno, M. Mazzocchi, M.C. Carotta, M. Sacerdoti, Enhanced Gas Sensing Properties of Different ZnO 3D Hierarchical Structures, *Advances Sci. Tech.* 99 (2017) 48-53.
- [25] M.C. Carotta, A. Cervi, V. di Natale, S. Gherardi, A. Giberti, V. Guidi, D. Puzzovio, B. Vendemiati, G. Martinelli, M. Sacerdoti, D. Calestani, A. Zappettini, M. Zha, L. Zanotti, ZnO gas sensors: A comparison between nanoparticles and nanotetrapods-based thick films, *Sens. Actuators B: Chem.* 137(1) (2009) 164-169.
- [26] A. Fioravanti, S. Morandi, M.C. Carotta, Chemoresistive gas sensors for sub-ppm acetone detection, *Procedia Eng.* 168 (2016) 485-488.

Figures and Captions

Figure 1 - XRD pattern of sample D.

Figure 2 - FE-SEM images of samples A, B, C and D.

Figure 3 - TEM (section a) and HR-TEM (sections b and c) images of sample A. In the inset of section b a magnification of the center part of the prism is reported to enlighten the presence of interference fringes.

Figure 4 - FT-IR spectra of samples A, B, C and D during interaction with a mixture acetone/O₂ (1:5, p_{acetone} = 5 mbar) at increasing temperature up to 400 °C.

Figure 5 - Conductance vs. temperature in dry air of samples A, B, C and D.

Figure 6 - Energy barrier dependence on temperature in dry air of the same films of Figure 5.

Figure 7 - Comparison between the energy barrier dependence on temperature in dry air and in a mixture of dry air and acetone (10 ppm) for samples A, B, C and D.

Figure 8 - Comparison of the electrical responses, at maximum response operating temperature, to 10 ppm of C₃H₆O (450 °C), C₂H₄O (500 °C), C₂H₅OH (550 °C) and NH₃ (450 °C) in dry air, for samples A, B, C and D.

Figure 9 - Electrical responses to 10 ppm of acetone obtained at different working temperatures for samples A, B, C and D.

Figure 10 – Dynamical responses to different concentrations of acetone. The samples in the legend are listed following the intensities of the responses from the highest to the lowest.

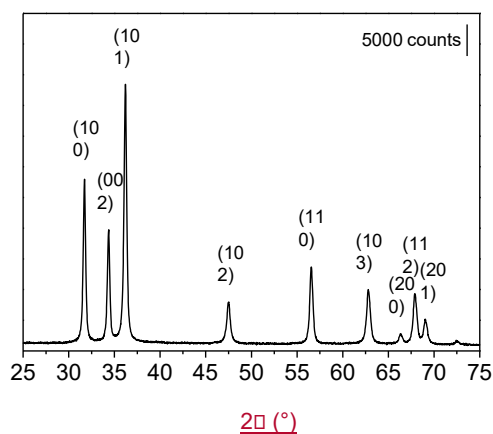


Figure 1

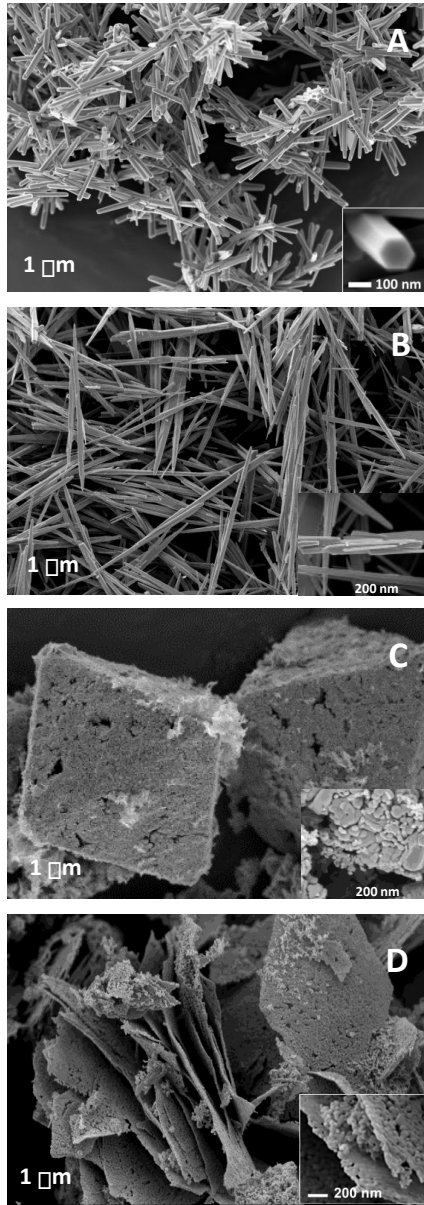


Figure 2

Formattato: Normale, Allineato a destra, Rientro: Sinistro: 0 cm, Destro 2.68 cm, SpazioDopo: 2.75 pt, Interlinea: multipla 1.08 ri

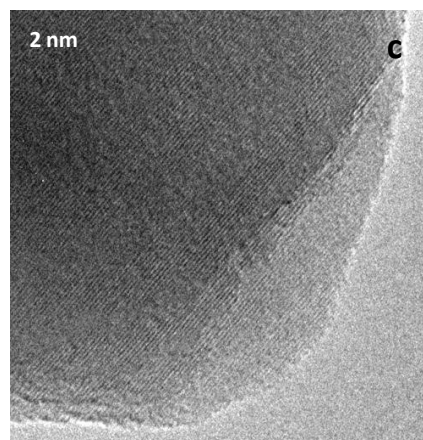
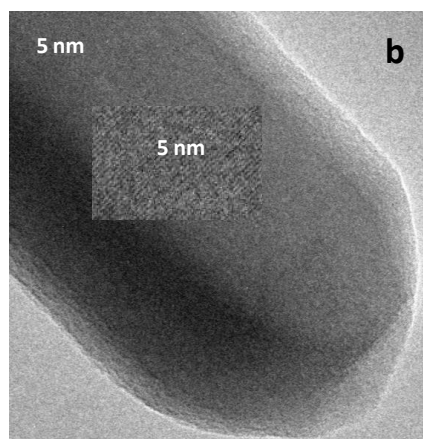
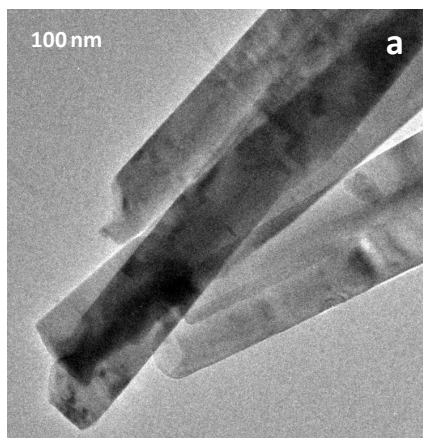


Figure 3

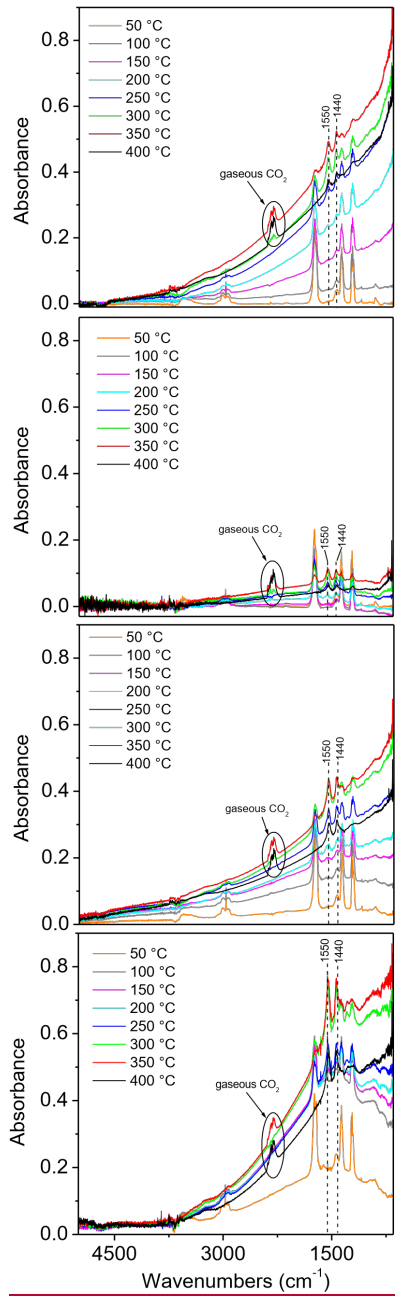


Figure 4

Formattato: Normale, Rientro: Sinistro: 4.62 cm,
SpazioDopo: 11.3 pt, Interlinea: multipla 1.08 ri

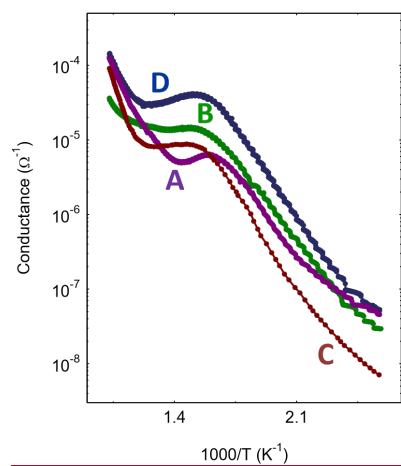


Figure 5

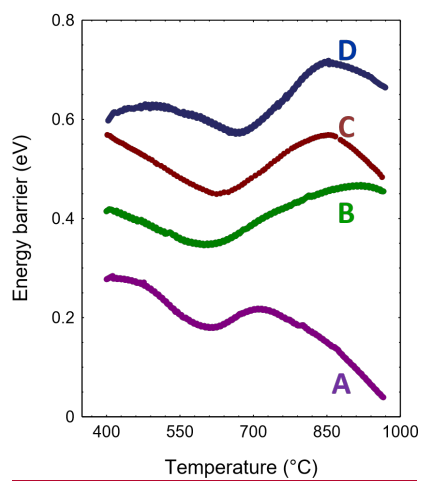


Figure 6

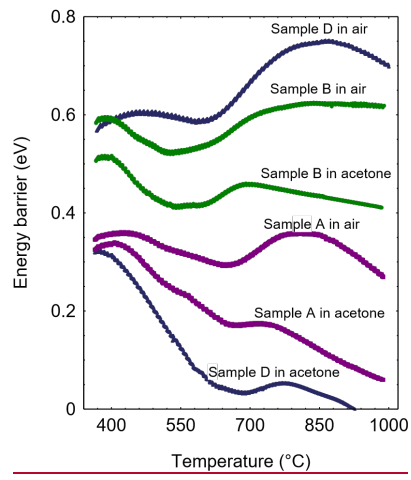


Figure 7

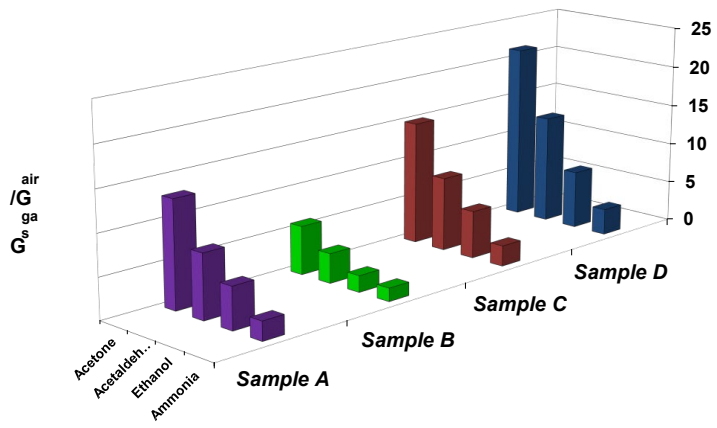


Figure 8

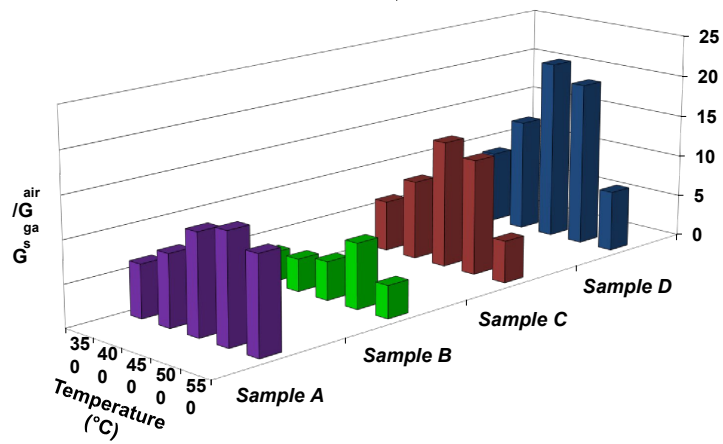


Figure 9

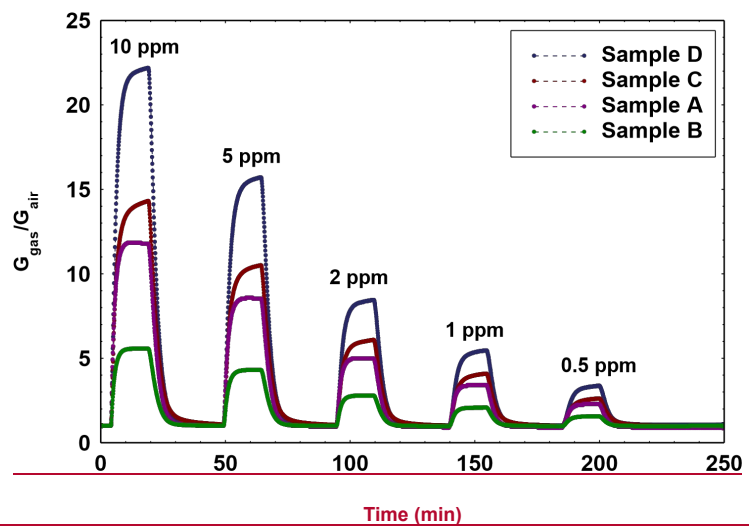


Figure 10